IEEE Access
Multidisciplinary | Rapid Review | Open Access Journal

Received May 26, 2018, accepted June 20, 2018, date of publication July 3, 2018, date of current version July 30, 2018.

Digital Object Identifier 10.1109/ACCESS.2018.2852663

Automatic Visual Defect Detection Using Texture Prior and Low-Rank Representation

QIZI HUANGPENG[1], HONG ZHANG[2], (Fellow, IEEE), XIANGRONG ZENG[1], AND WENWEI HUANG[3]

[1]Department of Systems Engineering, National University of Defense Technology, Changsha 410072, China
[2]Department of Computing Science, University of Alberta, Edmonton, AB T6G 2E8, Canada
[3]Department of Military Basic Education, National University of Defense Technology, Changsha 410072, China

Corresponding author: Qizi Huangpeng (hpqz19911215@163.com)

This work was supported in part by the National Nature Science Foundation of China under Grant 61602494 and in part by the National University of Defense Technology Foundation under Grant ZK16-03-16.

ABSTRACT Automatic surface detection for quality control has largely employed image processing techniques, for example in steel and fabric defect inspection. There are rising demands in the quality control industry for defective image analysis to fulfill its vital role in visual inspection. In this paper, we introduce an unsupervised method using a low-rank representation based on texture prior for detection of defects on natural surfaces and formulate the detection process as a novel weighted low-rank reconstruction model. The first step of the proposed method estimates the texture prior to a given image by constructing a texture prior map where higher values indicate a higher probability of abnormality. The second step of the proposed method detects the defect via low-rank decomposition with the help of the texture prior. Experiments on synthetic and real images show that the proposed method is superior in terms of detection accuracy and competitive in computational efficiency with respect to the state-of-the-art methods in surface defect detection research. This contribution is of particular interest for manufacturers (e.g., steel and fabric) for which defect detection largely relies on manual inspection.

INDEX TERMS Defect detection, low-rank representation, texture prior.

I. INTRODUCTION

Surface defect detection is an essential process in quality control of modern manufacturing industry, such as steel and fabric production [1], [2]. Surface inspection is necessary to detect defect and estimate product quality, to be compared with the product specification. In the worst case, defects can make the product functionally deficient or unusable, even some critical defects may lead to production interruption. Thus, an accurate and early defect detection is an important aspect of quality control. Traditionally, surface defect detection is performed manually. However, the accuracy of manual inspection is subjective, and the efficiency is limited. Automatic visual surface defect detection provides an attractive alternative. The literature for surface defect detection based on computer vision is vast, and the conventional methods can be divided into three categories, namely: statistical, spectral, and model-based [3].

The main idea of statistical methods is to divide an image into regions with distinct statistical texture characteristics. A large number of statistical texture features have been proposed, such as histogram statistics and texton. Histogram statistics methods are invariant to the rotation and translation, and also insensitive to a number of spatial distribution of the color pixels [4]. Despite the simplicity of the histogram methods, they have been successfully used in a number of actual applications. Textons refer to the basic micro-structures in natural images. If we regard an image as a composition of some image bases selected from an over-complete dictionary, then the image bases are generated by a number of texton elements [5]. In [6], it used texton feature to make simultaneous defect detection and classification on fabric defects. However, it is difficult to extract appropriate textons for defect detection on real fabric images due to the stochastic variations in the fabric structure.

In contrast, spectral methods extract surfact defects via transformation of the input image to the spectral domain and compute the energy of the filter responses. Reference [7] introduced a neighboring difference filtering (NDF) method that can separate the defective foreground from the background effectively. The novel filter is constructed by comparing the intensity of neighboring regions. Reference [8] designed a set of adaptive wavelet bases according to the

textile features, and fabric defects were detected using these special wavelet bases for filtering. Reference [9] proposed an effective fabric detection method based on Gabor filter, and it used the multi-scale Gabor filter to extract features and multiple directions from the fabric images. However, the filter selection in the spectral methods needs to be carefully solved in order to achieve good performance [10]. Otherwise, the detection results may fail.

Model-based methods detect the defect with modeling and decomposing techniques, such as fractal and autoregressive modeling. By studying the inherent characteristics of the woven fabrics, [11] combined five novel fractal features and the box-counting dimension to detect fabric defects. Reference [12] first used spatial autoregressive modeling for wood-grain texture analysis of hardwood images, and a circularly shifted correlation technique was developed to detect defects on the log images. However, the use of the model-based methods in real applications is limited because of computation complexity and unsatisfactory performance.

Deep learning (DL) methods have been achieving good performance on automatic visual defect detection in recent years. Reference [13] proposed a Fisher criterion-based stacked denoising autoencoder to classify the defectless and defective regions, and finally located the defect by subtraction and thresholding. Reference [14] presented a generic DL method that used a pre-trained network and transferred features to build classifier, then convolved the trained classifier over input image to make pixel-wise prediction. Reference [15] presented a supervised deep convolutional neural network that is trained to classify each image patch, and the defective regions are identified by dilation and thresholding. Although the detection results of the DL methods are great, they are rarely applied in real applications. The first reason is that the defect databases are generally too small to train a deep neural network, and the small scale of training data may lead to overfitting. The manufacture won't spend too much time to collect defective images at large scale, and it is also costly to label the images manually. Moreover, the main target of defect detection is to identify the defective region precisely. However, the DL use the learning strategy to extract features which are usually used for classify defects and bound defects region, most DL methods are still use traditional method such as filtering and thresholding to make detection.

In recent years, low-rank representation has been used for defect detection because it can estimate the low-rank and sparse matrix from the original image. The focus of defect detection is inspection of the defect area from the textured background accurately where the textured background and the foreground defects can be regarded as a low-rank and a sparse matrix, respectively. Reference [16] converted LCD surface defect detection into a problem of reconstruction of a corrupted low-rank matrix, and solved it using inexact augmented Lagrange multipliers algorithm. However the method can only solve LCD images with simple background, and cannot be extended to other applications. Reference [2] presented a robust principal component analysis (RPCA) model with noise terms to detect diverse defects in fabric images. NRPCA is a low-rank method which uses a modified RPCA model by adding a noise term. However, this method ignore the connectivity of sparse pixels, and thus cannot detect continuous defective regions. Meanwhile, NRPCA is sensitive to parameter setup. If the initial guess of parameters is not appropriate, the detection results might fail. Reference [17] presented a prior knowledge guided low-rank model and solved with least squares regression, it's called PLSR. It is also a RPCA-based low-rank method, and it uses F-norm to replace the nuclear norm and 2-norm in the original model. In fact, F-norm is not exactly the same as nuclear norm and 2-norm, so the detection results are not acceptable in some situations, especially in the detection of right angle and square corner. Moreover, the experiments show that the efficiency of PLSR is poor.

In this paper, we propose an unsupervised method using low-rank representation with texture prior to detect defects. We mainly focus on images with regular or near-regular surface texture. The framework of the proposed approach can be divided into two steps. The first step is to calculate the texture prior of the input image, to construct a texture prior map where higher values indicate higher probabilities of being in a defective region. The second step is to detect defects in low-rank representation with the texture prior map where we adopt a weighted contiguous outlier detection model. The main contributions of this paper include:

1. A weighted low-rank reconstruction (W-LRR) model is proposed to detect various defects from the structured background.
2. A texture prior map is integrated with the global structure via W-LRR model, which makes our algorithm accurate and robust.

II. DEFECT DETECTION BY LOW-RANK REPRESENTATION WITH TEXTURE PRIOR

A. CONSTRUCTION OF TEXTURE PRIOR MAP

A basic and reasonable assumption in the proposed method is that defects exhibit different textural characteristics from the background, i.e., their textures lie outside of the subspace of the background. To exploit this observation, we construct a texture prior map wherein pixels of input image with higher value in this map indicate higher probability of being defective pixels. Fig.1 summarizes the process of constructing the texture prior map.

Firstly, input image I is divided into several overlapping $m \times m$ patches. For each patch I_k, a feature descriptor f_k is calculated to describe its textural structure. Here, we use the Texton [6] as f_k. Given the texture descriptor f_k, we normalize it to create P_k for characterizing patch I_k, i.e.,

$$P_k = \frac{f_k - \min(\mathbf{f})}{\max(\mathbf{f}) - \min(\mathbf{f})} \tag{1}$$

where $\mathbf{f} = [f_1, f_2, \cdots, f_k]$.

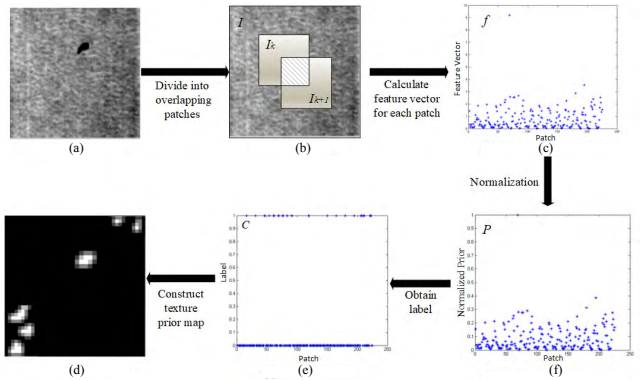

FIGURE 1. Process of the construction of texture prior map. (a) Defective image. (b) Segmentation. (c) Patch vs. Feature vector. (d) Patch vs. Normalized prior. (e) Patch vs. Label. (f) Texture prior mao.

In the next step, we use simple thresholding to divide P into two classes, with label 1 (defect) and 0 (non-defect), and the result is denoted as C, where for each patch $C_k \in \{0, 1\}$. Here, the threshold is set as $T = \text{std}(P)$. The patches whose feature value is lower than the threshold are marked as non-defect, and the other patches are marked as defect. Finally, we use prior C to construct the texture prior map. As shown in Fig.1(b), the pixels in image I can be separated into overlapping (e.g. grid section) and non-overlapping pixels (e.g. gray section). The texture prior map M for the non-overlapping pixel is defined as:

$$M(i,j) = C_k, \quad \text{if } I(i,j) \in I_k \tag{2}$$

As for the overlapping pixels, the texture prior map M is defined as the sum of C_n in the overlapping region:

$$M(i,j) = \sum_{n=k}^{k+s} C_n, \quad \text{if } I(i,j) \in I_k \cap I_{k+1} \cap \cdots \cap I_{k+s} \tag{3}$$

The final prior map is continuous, and the higher the probability for a region to be defective, the higher the value for a region. Fig.1(f) shows the texture prior map of a defective image, and the brighter pixels are potential defects. However, Fig.1(f) also shows that the texture prior maps can be quite inaccurate, and a defective region in the prior map tend to be larger than the actual size of the region. Consequently, we combined the texture prior and a low-rank model and propose to refine detective regions correctly with the help of a W-LRR model.

B. DEFECT DETECTION BY LOW-RANK REPRESENTATION

In this section, we focused on the detection of accurate defect regions in the low-ranking representation with texture prior. Suppose $I \in R^{m\times n}$ is a given image, and $B \in R^{m\times n}$ is a matrix that denotes the defect-free background with the same size as I. Assume $S \in \{0, 1\}^{m\times n}$ is a binary matrix representing the defective part in given image:

$$S_{i,j} = \begin{cases} 0, & \text{if } I_{i,j} \text{ is defect free background} \\ 1, & \text{if } I_{i,j} \text{ is defect ive foreground} \end{cases} \tag{4}$$

As described in [18], we use $P_S(X)$ to denote the orthogonal projection of a matrix X onto the linear space of matrices supported by S:

$$P_S(X)_{i,j} = \begin{cases} 0, & \text{if } S_{i,j} = 0 \\ X_{i,j}, & \text{if } S_{i,j} = 1 \end{cases} \tag{5}$$

$P_{S^\perp}(X)$ is the complementary projection, resulting to $P_{S^\perp}(X) + P_S(X) = X$. The goal is to estimate the defective regions from image I.

Assuming that defect-free regions of a surface consist of regular or near-regular textural pattern, texture features of these regions should be linearly correlated with each other and form a low-rank matrix B. Here, we do not make any additional assumptions on the background structure surface aside from low-rank properties. We only make the following constraint on B:

$$\text{rank}(B) \leq R \tag{6}$$

where R is a pre-defined constant.

However, the features of defective regions might destroy the regularity and cause textural changes that are not consistent with the low-rank background representation. This observation indicates that the defective regions are usually away from the subspace spanned by those of the defect-free regions. Thus, we regard these defective regions as outliers in low-rank representation. Generally, we have a prior knowledge that defective regions should be contiguous pixels with relatively small sizes. To incorporate the aforementioned information, we could adopt Markov random field (MRF) to model the spatial continuity of the outliers support S according to [19]. Specifically, suppose $\mathbf{G} = (\mathbf{V}, \mathbf{E})$ is a graph that denotes the image, where $\mathbf{V} = \{1, \cdots, m \times n\}$ represents the pixels in I, and $\mathbf{E}$ represents the edges connecting neighboring pixels; then the energy function of S can be given by the Ising model [19] as follows:

$$\sum_{ij\in\mathbf{V}} e_{ij}(S_{ij}) + \sum_{(ij,kl)\in\mathbf{E}} \lambda_{ij,kl} \left|S_{ij} - S_{kl}\right| \tag{7}$$

where e_{ij} is a unary potential function for S_{ij} to be 0 or 1, and the parameter $\lambda_{ij,kl} > 0$ constraints the dependent strength between S_{ij} and S_{kl}. Suppose the sparse defective region tend to be $S_{ij} = 0$, then we can define the unary function e_{ij} as:

$$e_{ij}(S_{ij}) = \begin{cases} 0, & \text{if } S_{ij} = 0 \\ \lambda_{ij}, & \text{if } S_{ij} = 1 \end{cases} \tag{8}$$

where, $\lambda_{ij} > 0$ could penalize the pixel when $S_{ij} = 1$. The parameters λ_{ij} and $\lambda_{ij,kl}$ are kept constant at all pixels when we do not make any prior assumptions about locations, sizes, shapes, or the number of defective regions. However, because of the texture prior map available in our method, we can combine this prior information into the foreground model. The details will be given in the next section.

C. W-LRR MODEL

Taking noise into consideration, we assume that $I_{ij} = B_{ij} + \varepsilon_{ij}$ in the defect-free background region, where $S_{ij} = 0$. Here, ε_{ij} denotes Gaussian noise. Then we can model $I_{ij} \sim N(B_{ij}, \sigma_1^2)$, where σ_1 is the standard deviation of Gaussian noise ε_{ij}. As a result, B_{ij} should be the best fitting to I_{ij} when $S_{ij} = 0$. However for the defective regions, the regular or near-regular pattern of the background is changed by the defect. Thus, I_{ij} should be equal to the intensity of the defect. If we do not have any prior knowledge about the location, size and appearance of the defect, I_{ij} is not constrained when $S_{ij} = 1$. In this situation, the defective image can be decomposed into a defect-free background and a defective foreground by LRR model according to [18]:

$$\min_{B,S} \frac{1}{2} \sum_{ij:S_{ij}=0} (I_{ij} - B_{ij})^2 + \beta \sum_{ij} S_{ij} + \gamma \sum_{(ij,kl)\in\mathbf{E}} \left| S_{ij} - S_{kl} \right| \quad \text{s.t. } \operatorname{rank}(B) \le R \tag{9}$$

However, since we have already estimated the prior knowledge of the defect before, we can resort to the texture prior map to guide the defect by suppressing the defect-free background. Therefore, an effective weighting matrix $W(i, j)$ is constructed by the texture prior map, and introduced to LRR to help low rank decomposition. In the weighting matrix $W(i, j)$, a large value should be set when pixel $I(i, j)$ is considered as a defect-free region, because we want to penalize the elements of $S_{ij} = 0$. As in texture prior map, a large value of prior map $M(i, j)$ indicates a high possibility of a pixel to be defective. Thus, the weighting matrix $W(i, j)$ corresponding to texture prior map $M(i, j)$ is defined as following:

$$W(i, j) = \exp(-\frac{M(i, j)}{\sigma_2^2}) \tag{10}$$

where σ_2 is the standard deviation of texture prior map $M(i, j)$.

Combining the defect-free background, defective foreground and weighting matrix, we propose the W-LRR model for estimating the defects S_{ij} and the texture background B_{ij} as following:

$$\min_{B,S} \frac{1}{2} \sum_{ij:S_{ij}=0} (I_{ij} - B_{ij})^2 + \beta \sum_{ij} W_{ij} \cdot S_{ij} + \gamma \sum_{(ij,kl)\in\mathbf{E}} \left| W_{ij} \cdot S_{ij} - W_{kl} \cdot S_{kl} \right| \quad \text{s.t. } \operatorname{rank}(B) \le R \tag{11}$$

The W-LRR model imposes that the defect-free background should be a low-rank matrix and fit most of the observed pixels in the least-squares condition, except for the defects that are contiguous as well as sparse. Benefitting from the weighting matrix, the detection results obtained by the W-LRR model are well-defined and accurate.

According to [19], the rank operator on B can be relaxed with the nuclear norm $\|B\|_*$ and make the W-LRR model effective. To simplify, (10) is reformulated into a dual form by taking matrix operators as follows:

$$\min_{B,S} \frac{1}{2} \left\| P_{S^\perp}(I - B) \right\|_F^2 + \alpha \|B\|_* + \beta \|W \cdot S\|_1 + \gamma \|\Psi(W \cdot S)\|_1 \tag{12}$$

where Ψ $(W \cdot S)$ represents the difference between neighboring pixels, and encourages connectedness of defective outliers. Here α is a positive parameter that could control the complexity of the background according to constant R. The setup of parameters α, β, γ and R, and the solution to this energy function will be discussed in the next section.

III. ALGORITHMS

A. AESTIMATION OF B and S

The energy function in (12) is non-convex, and is typically solved by alternatively minimizing two steps: minimization of defect-free background B and defective foreground S. The solution is well-known and included here for the completeness of presentation.

1. Estimation of the low-rank matrix B:
   To update B with the fixed $\hat{S}$, we rewrite (12) into:
   $$\min_{B} \frac{1}{2} \left\| P_{\hat{S}^\perp}(I - B) \right\|_F^2 + \alpha \|B\|_* \tag{13}$$
   The optimization of B can be computed exactly by soft-impute algorithm as described in [20], and the optimal solution to (13) can be obtained by iteratively using:
   $$\hat{B} \leftarrow \theta_\alpha(P_{\hat{S}^\perp}(I) + P_{S^\perp}(B))$$
   $\theta_\alpha(P_{\hat{S}^\perp}(I) + P_{S^\perp}(B))$ means the singular value thresholding. We can perform SVD on θ_α, i.e.,
   $$\theta_\alpha(P_{\hat{S}^\perp}(I) + P_{S^\perp}(B)) = U \sum_{\alpha} V^T \tag{14}$$
   and $\sum_\alpha = \operatorname{sign}(X) \max \odot \left\{ |X| - \frac{1}{\lambda}, 0 \right\}$ with $X = (P_{\hat{S}^\perp}(I) + P_{S^\perp}(B))$.
2. Estimation of the sparse matrix S:
   With the fixed $\hat{B}$ solution to S can be obtained with the following minimization:
   $$\begin{aligned} &\min_{S} \frac{1}{2} \left\| P_{S^\perp}(I - \hat{B}) \right\|_F^2 + \beta \|W \cdot S\|_1 + \gamma \|\Psi(W \cdot S)\|_1 \\ &= \min_{S} \frac{1}{2} \sum_{ij} (I_{ij} - \hat{B}_{ij})(1 - S_{ij}) \\ &\quad + \beta \sum_{ij} W_{ij} \cdot S_{ij} + \gamma \|\Psi(W \cdot S)\|_1 \\ &= \min_{S} \sum_{ij} (\beta W_{ij} - \frac{1}{2}(I_{ij} - \hat{B}_{ij})^2) S_{ij} \\ &\quad + \gamma \|\Psi(W \cdot S)\|_1 + C \end{aligned} \tag{15}$$
   where $C = \frac{1}{2}(I_{ij} - \hat{B}_{ij})^2$. Equation (15) is in the standard form of the first-order MRFs with binary labels, and it can be solved efficiently using graph cuts as described in [21].

B. ADAPTIVE PARAMETER SELECTION

The parameter selection problem is crucial in low-rank representation. However, in some low-rank representation methods, the rank of the background is forced to be small. Furthermore, the parameters (α, β, γ) are usually fixed empirically. Detection results are greatly influenced by parameter setting, and inaccurate estimation parameters may lead to an inaccurate sparsity calculation. In our method, we use an online parameter estimation procedure to tackle the problem of parameter selection.

The parameter α in (12) controls the complexity of the background structure, and a larger α will result in a smaller $\|B\|_*$. In the proposed method, we initialize the rank of the defect-free background by $R = \sqrt{\min(m, n)}$. We then start from a large α and continue to update it by a factor $\rho_1 < 1$ in each iteration until $\text{rank}(\hat{B}) > R$. We will then use $\hat{B}$ as the estimated background model. According to [18], we initialize α to be the second largest singular value of I and define$\rho_1 = 1/\sqrt{2}$. Parameter β in (12) is positive for penalty and constraints the sparsity of the defective regions. We empirically set $\beta = 1.25/\|I\|_2$and then reduce β by a factor $\rho_2 = 0.5$ after each iteration. Here γ controls the connectedness of defective outliers. We set $\gamma = \beta$ and 5β for simulation and real sequences, respectively.

With the above parameter setting, our optimization algorithm can guarantee the convergence of the W-LRR model. Furthermore, we can manually set lower bounds of (α, β, γ) to end the iteration. In our experiments, our method generally converges in about 15 iterations for a convergence precision of 10^{-5}. The process of solving Eq. (12) is summarized in Algorithm 1.

Algorithm 1 For Solving (12)

1. **input**: $I, W \in R^{m\times n}$
2. **initialization**: $\alpha, \beta, \gamma, R, B_0 \leftarrow I, S_0 \leftarrow 0$
3. **while no converge do**
4. $\hat{B} \leftarrow \theta_\alpha(P_{\hat{S}^\perp}(I) + P_{S^\perp}(\hat{B}))S$
5. **if** $\text{rank}(B) \le R$
6. $\alpha = \rho_1\alpha$
7. **go to step 3**
8. **endif**
9. $\beta \leftarrow \rho_2\beta$
10. $\hat{S} \leftarrow \arg\min_S \sum_{ij}(\beta W_{ij} - \frac{1}{2}(I_{ij} - \hat{B}_{ij})^2)S_{ij}$ $+\gamma \|\Psi\ (W \cdot S)\|_1$
11. **until** convergence
12. **return**: $\hat{S}$ and $\hat{B}$

C. IMPLEMENTATION DETAILS

With the explanation of the optimization procedure in the previous section, we can now define our defect detection algorithm, as described in Algorithm 2 below. First, parameters are initialized. Then, from a given input image, texture prior is calculated, in Step 1 of Algorithm 2. Finally, the defective regions in the low-rank representation are detected with the help of texture prior, in Step 2 of Algorithm 2. The defective regions are generated from the foreground mask that is computed by the low-rank optimization.

Algorithm 2 For Surface Defect Detection

1. **Initialization**: Parameters setup.
2. **Input**: Observed defective image I.
3. **Step 1**: Obtain texture prior knowledge:
Divide I into several overlapping patches I_k, extract texture feature f_k from each patch, and then calculate defective prior P_k.
Obtain label prior C with automatic thresholding, and construct the texture prior map M.
Calculate weight matrix W corresponding to M with $W(i, j) = \exp(-M(i, j)/\sigma_2^2)$.
4. **Step 2**: Estimation of defective foreground S and background B via low-rank representation (solved with **Algorithm 1**):
Update the B as $\hat{B} \leftarrow \theta_\alpha(P_{\hat{S}^\perp}(I) + P_{S^\perp}(\hat{B}))$.
Update the S as:

$$\hat{S} \leftarrow \arg\min_S \sum_{ij}(\beta W_{ij} - \frac{1}{2}(I_{ij} - \hat{B}_{ij})^2)S_{ij} + \gamma\|\Psi(W \cdot S)\|_1$$

5. **Output:** Defective foreground $\hat{S}$ and the defect-free background $\hat{B}$.

IV. EXPERIMENTS AND ANALYSIS

In this section, a synthetic experiment and a real experiment are performed to evaluate the performance of the proposed method against the state-of-the-art competing methods. In the first experiment, we examine the effects of the patch size of texture feature extraction and signal to noise ratio (SNR) using synthetic images, with the goal to select a proper patch size for the next two experiments. We also compared the proposed method with five state-of-the-art methods: Texton-based (TB)[6], prior knowledge guided least squares regression (PLSR) [17], singular value decomposition (SVD) [22], noise robust principal component analysis (NRPCA) [2], and neighboring difference filter (NDF) [7]. Another experiment is carried out on a benchmark fabric defect dataset, which contains dot-, box-, and star-patterned background and different defect types. Detection performance of the proposed method is also compared with the competing methods. All experiments are performed by MATLAB with an Intel(R) Core(TM) 2.00 GHz processor. Both the defect detection accuracy and the computational efficiency of all the methods were measured. The parameters of the proposed method are first optimized, and those in the state-of-the-art methods are the same as in the original studies.

A set of evaluating indexes including accuracy (ACC), F-measure, true positive rate (TPR), false positive rate (FPR), and positive predictive value (PPV) are employed to quantify the detection accuracy [23]. The definition of ACC,

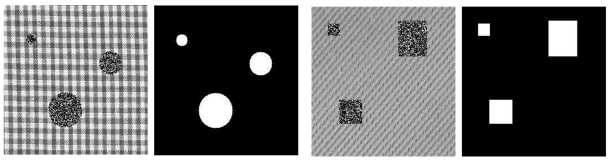

FIGURE 2. Synthesized defective images and ground truth.

TABLE 1. Computational accuracies with different patch sizes.

Patch	ACC	F-measure	PPV	TPR	FPR	Time
6×6	0.996	0.975	1.000	0.952	1.218E-04	1.343
8×8	**0.997**	**0.977**	**1.000**	**0.955**	*4.941E-05*	*1.338*
16×16	0.991	0.937	1.000	0.882	1.218E-04	1.336
32×32	0.993	0.929	1.000	0.899	8.987E-05	1.331
64×64	0.982	0.863	1.000	0.763	**0**	**1.273**

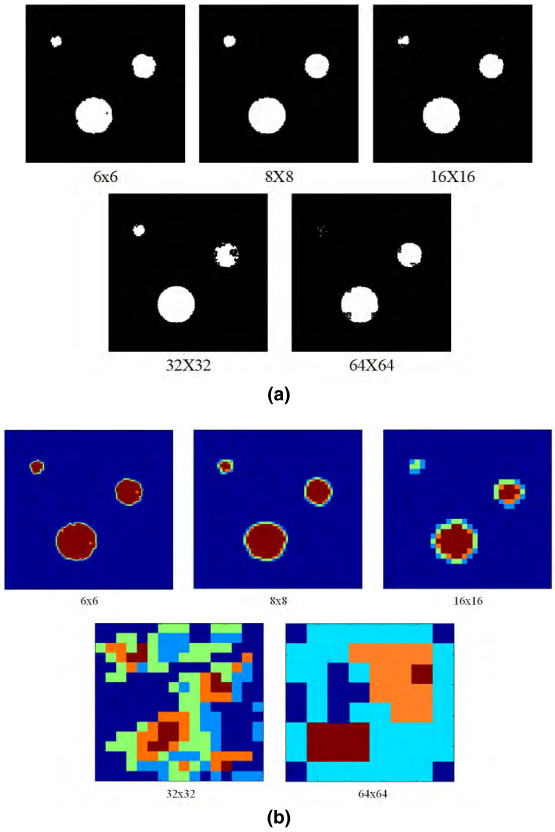

FIGURE 3. (a) Detection results under 30 dB using five different patch sizes; (b) Prior map under 30 dB using five different patch sizes.

F-measure, TPR, FPR, and PPV are described as following:

$$\mathrm{ACC} = \frac{TP + TN}{TP + TN + FP + FN}$$
$$TPR = \frac{TP}{TP + FN}$$
$$FPR = \frac{FP}{FP + TN}$$
$$PPV = \frac{TP}{TP + FP}$$
$$F - \mathrm{measure} = \frac{2 \times PPV \times TPR}{(PPV + TPR)}$$

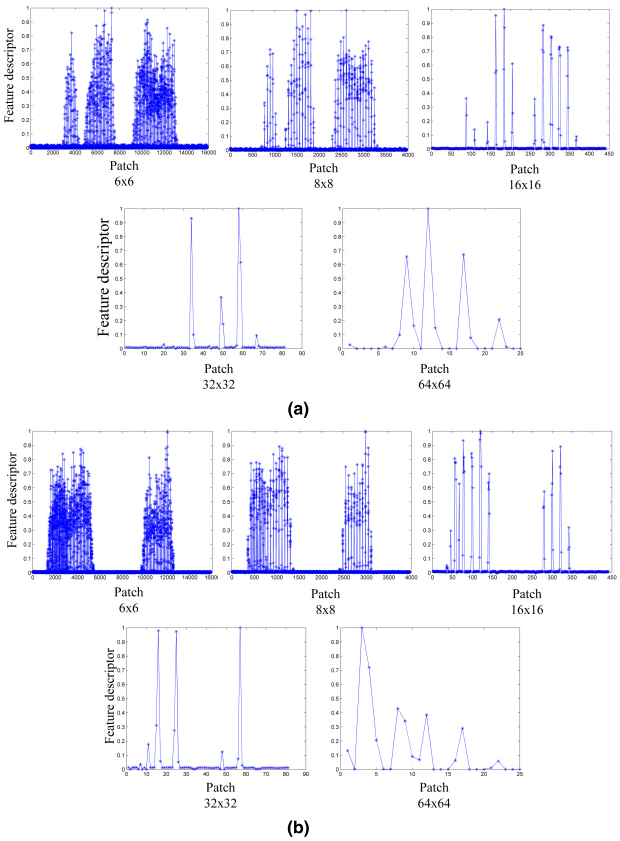

FIGURE 4. (a) Patch vs. feature descriptor of the circular defective images under 30 dB using the five different patch sizes; (b) Patch vs. feature descriptor of the square defective images under 30 dB using the five different patch sizes.

A. SYNTHETIC NOISY IMAGES

Two 256×256 pixels synthesized defective images, and their ground truth are shown in Fig.2. The textured background is corrupted with circles or squares of different sizes, and salt-and-pepper noise is added first to the defective regions, before additive Gaussian noise with SNR between 10 dB and 50 dB is introduced to the entire image. Ten synthetic noise defective images are tested to study the capability of the proposed method against corruption.

1) INFLUENCE OF PATCH SIZE ON DETECTION PERFORMANCE

Through the experiments, we found that the detection results of the proposed method are influenced by the patch size within which texture features are computed. To find the optimal patch size, we evaluated five settings at: 6×6, 8×8, 16×16, 32×32, 64×64 pixels, and an overlapping size is kept at 4×4.

The computational accuracies are listed in Table 1, and the best results are marked in bold. We can see that the patch size does affect the defect detection performance, and the 8×8 patch size gets 4 of the highest scores and 2 second scores. Though the 64×64 achieves higher scores than

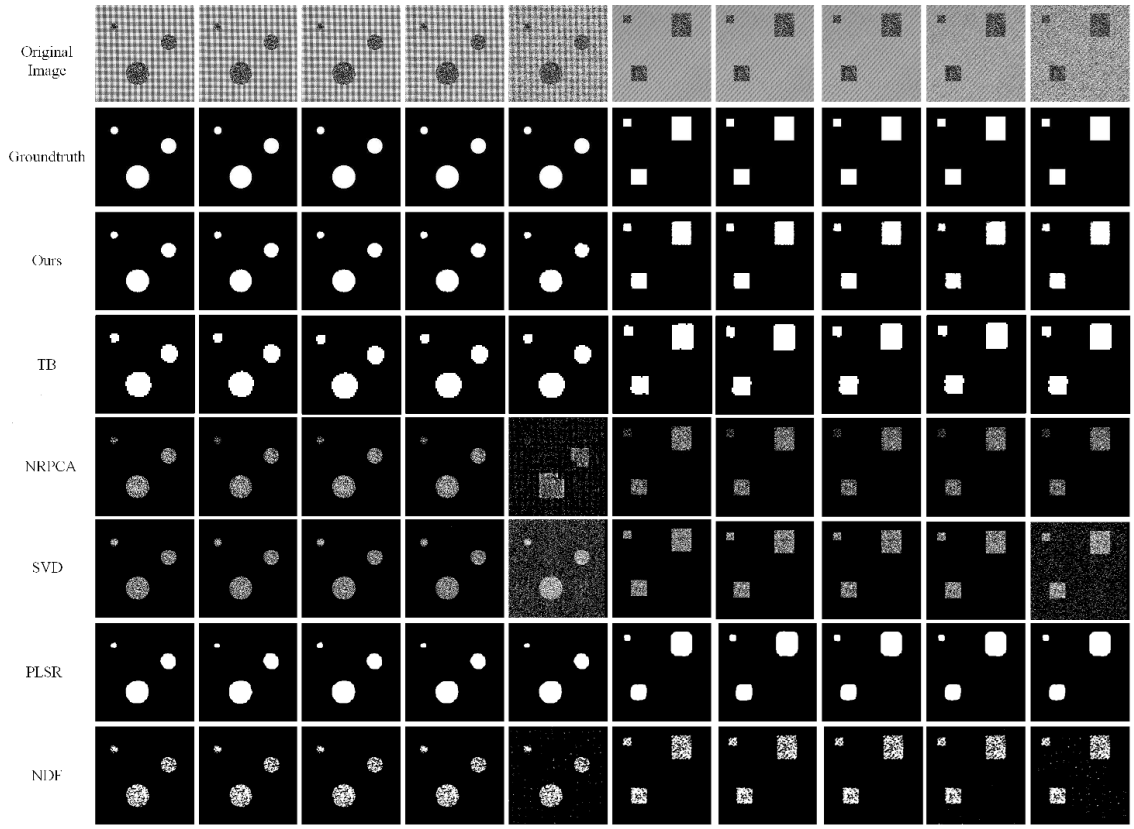

FIGURE 5. Detection results for synthetic noise images.

the 8 × 8 on FPR, its TPR is nearly 20% lower than the 8 × 8. The F-measure is reduced when we increase the patch size from 8 × 8 to 64 × 64. However, the detection performance of 8 × 8 is better than that of 6 × 6, indicating a smaller patch does not necessarily produce a more accurate result. Table 1 also shows the average computational time in seconds for five different patch sizes. The computational time decreases slowly when the patch size increases.

In general, the optimal patch size should depend on the size of defective regions. For example, Fig. 3(a) shows the detection results of proposed method under 30 dB using the five different patch sizes. Three circular defective regions were in the background, and the diameter of these three circles are 15, 30, and 60 pixels denoted as C1 to C3 respectively. All the circles can be detected accurately by 6 × 6 and 8 × 8 patch sizes, with 8 × 8 patch having a slight performance edge. The 16 × 16 patch size could detect C2 and C3 accurately, which are larger than the patch size. Though C1 can be detected, it is not precise. The 32 × 32 patch size could accurately detect C3, but only roughly detects C1 and C2. For the 64 × 64 patch size, only C3 can be detected accurately. The difference in performance is clearly caused by the quality of the prior map shown in Fig. 3(b). Although the low-rank optimization operation can overcome the deficiency of the prior map to some extent, a good prior map is critical for the overall algorithm. In summary, the patch size should not be larger

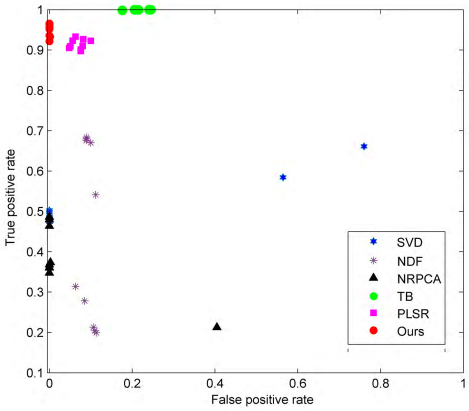

FIGURE 6. The FPR-TPR graphs of detected results.

than the area of defect regions. In addition, an extremely small patch size can lead to an over-segmented prior map and thereby reduce the accuracy of detection.

Another consideration about the patch size is the texture resolution. For texture with regular motifs, the size of a patch should be chosen adequately; otherwise, the prior map can be erroneous. Fig. 4(a) shows the relationship of patch number vs. feature descriptor value of the circular defective images under 30 dB using the five different patch sizes. Most patches of the defective image are background, and the real

TABLE 2. Average numerical detection results of different methods with different SNR values.

SNR	Method	ACC	F-measure	PPV	TPR	FPR	time
50	NRPC	0.95	0.589	**1**	0.42	**0**	0.861
	PLSR	0.99	0.941	0.95	0.92	0.04	29.30
	TB	0.98	0.891	0.80	**0.99**	0.19	0.744
	NDF	0.95	0.554	0.90	0.44	0.09	**0.008**
	SVD	0.96	0.659	**1**	0.49	**0**	1.587
	Ours	**0.99**	**0.982**	**1**	*0.96*	**0**	*1.475*
40	NRPC	0.95	0.592	**1**	0.42	**0**	0.805
	PLSR	0.99	0.938	0.96	0.91	0.03	29.37
	TB	0.97	0.876	0.77	**1**	0.22	0.671
	NDF	0.95	0.552	0.89	0.43	0.10	**0.008**
	SVD	0.96	0.659	**1**	0.49	**0**	1.642
	Ours	**0.99**	**0.982**	**1**	*0.96*	**0**	*1.429*
30	NRPC	0.95	0.585	**1**	0.41	**0**	0.813
	PLSR	0.99	0.94	0.95	0.92	0.04	29.47
	TB	0.97	0.874	0.77	**1**	0.22	0.666
	NDF	0.95	0.563	0.90	0.44	0.09	**0.011**
	SVD	0.96	0.661	**1**	0.49	**0**	1.619
	Ours	**0.99**	**0.978**	**1**	*0.95*	**0**	*1.568*
20	NRPC	0.95	0.586	**1**	0.41	**0**	0.848
	PLSR	0.99	0.944	0.95	0.93	0.04	28.92
	TB	0.97	0.875	0.77	**1**	0.22	0.701
	NDF	0.95	0.598	**1**	0.47	0.09	**0.015**
	SVD	0.96	0.644	1	0.47	**0**	1.661
	Ours	**0.99**	**0.972**	**1**	*0.94*	**0**	*1.256*
10	NRPC	0.94	0.428	0.79	0.29	0.20	1.014
	PLSR	0.99	0.936	0.93	0.94	0.06	28.61
	TB	0.97	0.875	0.77	**1**	0.22	0.687
	NDF	0.95	0.571	0.91	0.42	0.08	**0.231**
	SVD	0.87	0.425	0.33	0.62	0.66	1.741
	Ours	**0.99**	**0.962**	**0.99**	*0.92*	**0.00**	*0.987*

TABLE 3. Average numerical detection results of different patterns of fabric images.

Pattern	Method	ACC	F-measure	PPV	TPR	FPR	time
Box-	NRPCA	0.99	0.33	0.57	0.24	0.43	0.95
	PLSR	0.96	0.22	0.16	0.24	0.84	34.84
	TB	0.78	0.2	0.14	0.6	0.86	0.25
	NDF	0.98	0.33	0.34	0.35	0.66	**0.04**
	SVD	0.77	0.08	0.04	0.68	0.96	1.65
	Ours	**0.99**	**0.68**	**0.65**	**0.73**	**0.35**	*0.79*
Dot-	NRPCA	0.91	0.36	0.67	0.26	0.33	0.95
	PLSR	0.9	0.47	0.54	0.55	0.46	29.99
	TB	0.91	0.3	0.19	0.68	0.81	0.28
	NDF	0.93	0.42	0.48	0.45	0.52	**0.05**
	SVD	0.65	0.16	0.11	0.69	0.89	1.78
	Ours	**0.98**	**0.77**	**0.77**	**0.84**	**0.23**	*0.83*
Star-	NRPCA	0.98	0.26	0.54	0.23	0.46	0.93
	PLSR	0.99	0.42	0.39	0.52	0.61	29.31
	TB	0.99	0.55	0.46	**0.69**	0.54	0.25
	NDF	0.98	0.33	0.32	0.47	0.68	**0.05**
	SVD	0.8	0.1	0.07	0.47	0.93	1.72
	Ours	**0.99**	**0.58**	**0.65**	*0.6*	**0.35**	*0.81*

defective regions only take small parts. Accordingly, we can see from the figure that in all conditions, most of the points lie between [0 0.1], which corresponds to the background. The remaining parts might be regarded as potential defective patch. The relationship of patch number vs. feature descriptor value of the square defective images under 30 dB using different patch sizes are shown in Fig. 4(b). Although the texture background of this two synthesized defective images are different, their change regulations are basically consistent. In all set-ups, the feature value of most patches lie between [0 0.1], which corresponding to the texture background. The remaining patches also might indicate potential defective regions.

As a result, the influence of texture resolution on the choice of patch size is not serious. Because in general conditions, the defective regions represent a small portion of the input image, and most of patches are still in the subspace of background, no matter how we choose the patch size. Thus, we can distinguish the defective patch from the background patch by thresholding. Thresholding is used for the purpose of removing the textured background and for defect detection. With the overlapping strategy described before, we can finally get the prior map. However, a large patch size may lead to the identified defect area far greater than the actual defect area, which means it cannot get a good prior map. On the other hand, as mentioned before, an extremely small patch size may lead to over-segmented and low computing efficiency. In many applications, such as [13], the patch size is chosen as 8×8. Through the above analysis, we think 8×8 is a suitable setting, and use it in subsequent experiments.

2) COMPARISON WITH THE COMPETING METHODS

To prove the proposed method is robust in noise conditions, we compare it with five unsupervised detection methods under different SNR values. The proposed method here uses a patch size of 8×8 with 4×4 overlapping. The detection results are shown in Fig. 5. The first row is the original images. The five images on the left are synthetic images with circular defects with SNR from 50 dB to 10 dB, and the five images on the right are with square defects with the same SNR values. The second row is the ground truth. The results of the proposed method, TB, NRPCA, SVD, PLSR, and NDF are shown in rows 3 to 9. The defective outliers S calculated in our method can be regarded as the final result and does not need threshold. For the competing methods that are not based on the low-rank representation, their outputs are usually not binary, and we therefore use an adaptive threshold on their outputs to obtain the final detection results. To make a quantitative comparison, we also calculate the ACC, F-measure, PPV, TPR and FPR of the above methods under

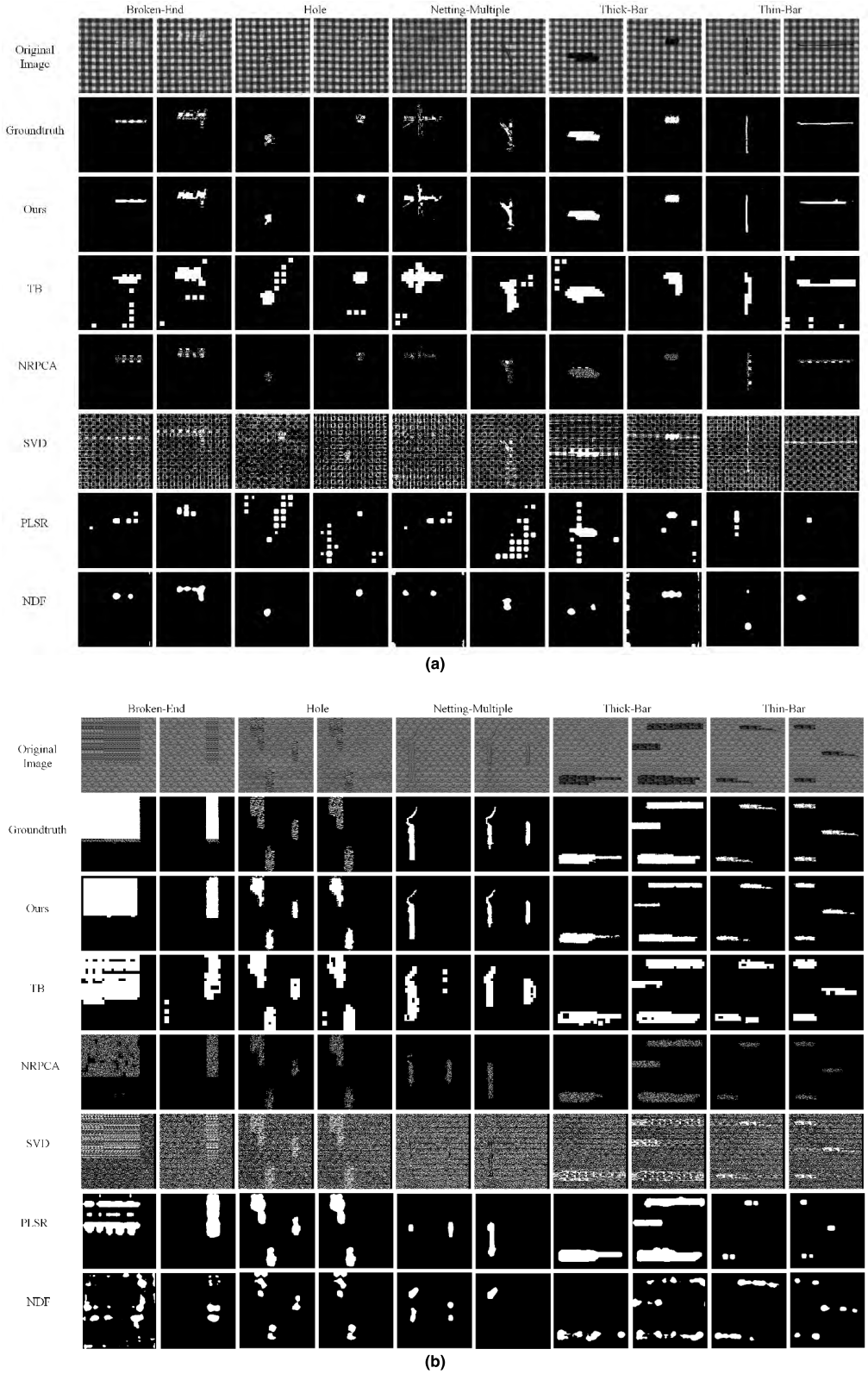

FIGURE 7. Detection results for the three patterned fabric defective images. (a) Detection results for box-patterned fabric images. (b) Detection results for dot-patterned fabric images. (c) Detection results for star-patterned fabric images.

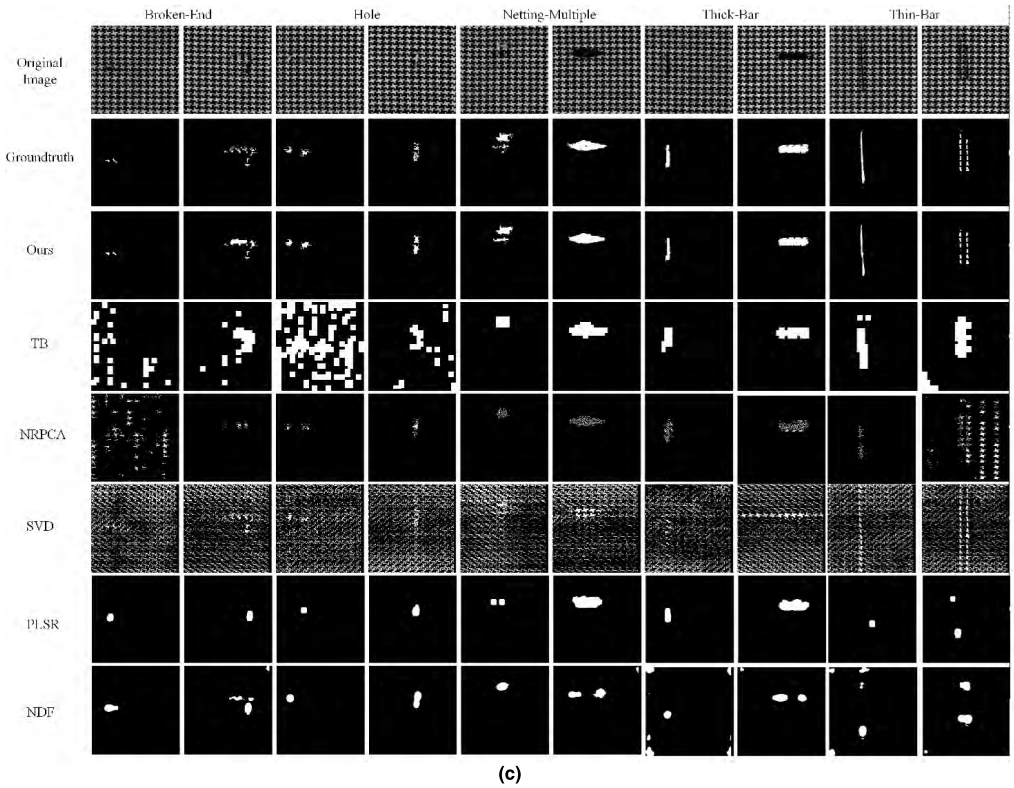

FIGURE 7. *(Continued.)* **Detection results for the three patterned fabric defective images. (a) Detection results for box-patterned fabric images. (b) Detection results for dot-patterned fabric images. (c) Detection results for star-patterned fabric images.**

different SNR. Table 2 shows the detection results and the best results are marked in bold.

TB is a statistical approach using texton as the feature descriptor to extract defective regions. The main difference between TB and the proposed method is that TB does not have a low-rank refinement step. Although its TPRs are appropriate, the FPRs are relatively low, indicating that many fake defects have been found by TB. SVD is a traditional low-rank method without texture prior, and in case of large noise, its detection results have numerous false positives, as shown in Fig. 5. NDF is a filtering method that comparing the intensity of neighboring regions. Even it can detect most defective regions but generates a considerable amount of fake points in high noise level. NRPCA is a low-rank method which uses a modified RPCA model by adding a noise term. However, this method ignore the connectivity of sparse, thus cannot detect continuous defective regions. We can see from the Table 2 that the TPRs is not high enough when compared with other methods, which means many defective regions are not identified with NRPCA. PLSR is also a RPCA-based low-rank method, and it uses F-norm to replace the nuclear norm and 2-norm in the original model. The detection results are stable under different noise conditions, but its efficiency is relatively low. At the same time, its detection performance of square defects is not good. As shown in the figure, the four corners of a square cannot be identified effectively. As for the proposed method, TPRs are generally higher than the competing method while FPRs are also typically the highest among all testing. It demonstrates that our method performs better than the other methods, especially at high-noise level.

To distinguish the effectiveness of the proposed method and the other methods visually, we plot the FPR-TPR graphs in Fig.6 for all synthetic noisy images. It illustrates that the proposed method can provide good detected results in the sense of the FPR-TPR graphs.

B. ON BENCHMARK FABRIC IMAGES

In order to make a more comprehensive comparison, we conduct a challenging experiment on a benchmark fabric database [24]. We have the databases of 256 × 256 fabric images belonging to three patterns: dot-, star- and box-patterned fabrics, and each patterned has 25 defect-free and 25 defective samples. There are five types of defect appear in the defective samples that include broken-end, hole, netting-multiple, thick-bar and thin-bar. All the defective fabric images have corresponding ground-truth.

Table 3 lists the results of all the competing methods, and the best results are marked in bold. Some remarks can be drawn from Table 3 as follows: (1) most ACCs of detected results by competing methods are higher than 65%, and the proposed method achieved all ACCs greater than 98%; (2) the F-measures obtained by the proposed method are much

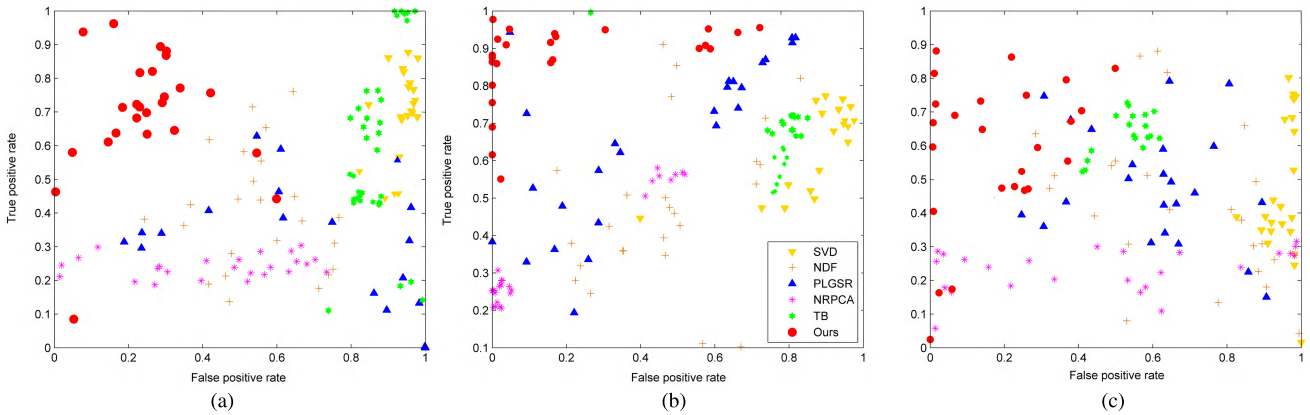

FIGURE 8. The FPR-TPR graphs for three pattern fabric images .(a) Box-pattern. (b) Dot-pattern. (c) Star-pattern.

higher than those by competing methods; (3) only the proposed method and NRPCA have PPVs higher than 65%, and our method gets the highest scores in PPV; (4) the proposed method obtains the highest TPR for box- as well as dot-patterned and perform little inferior in star-pattern compared with TB, and all our TPRs larger than 60% for three pattern; (5) the FPRs of the proposed method are typically the highest among all testing methods; (6) most computational time of testing methods are less than 1 second except for PLSR and SVD, and the proposed method can handle per image no more than 0.9 seconds.

Fig. 7 shows samples of detected results by all testing methods, and Fig. 7(a)-(c) are box-, dot-, and star-pattern, respectively. Total five types of defect are given, and there are two samples for each defect type. According to the detected results, we can draw similar qualitative conclusions as in the previous experiments. In detail, TB can detect the defective regions roughly but cannot extract defects accurately, especially in star pattern. This is because the FPRs of TB are too high that detected regions are larger than the real defects. SVD can produce detections in a number of cases; however, the background is not completely removed in most situations. Their results of both quantitative evaluation are not ideal, too. As for NRPCA, we can see from the Table 3 that its TPRs is no larger than 0.3, which means many defective regions are not identified. In fact, we found that NRPCA can outline the defective regions accurately, but it inspects the defects as discrete regions. Because the defects in the ground-truths are labeled in dilated forms, the detected results are not ideal. NDF can detect holes and broken-ends effectively, but the other types of defects are difficult to identify. PLSR could outline the defective regions accurately in some cases, especially for holes, netting-multiples, and thick-bars defects in the dot-patterned fabrics. However, there are a large number of false positives in box-pattern, and many defects are not identified in star-pattern. In short, the proposed method achieves superior performances among all testing methods, both in visualized detections and numerical results for three patterned fabrics.

To distinguish the effectiveness of the proposed method and the competing methods visually, we plot the FPR-TPR graphs of defective fabric images in Fig. 8 for three patterns, and Fig. 8 (a)-(c) are box-, dot-, and star-pattern, respectively. It illustrates that the proposed method can provide the best results in star- and dot-pattern among all testing methods with high TPRs and low FPRs, obviously. As for box-pattern, the TPRs of the proposed method are not high, especially when compared with TB. However, the FPRs are far lower than the other methods.

V. CONCLUSION

In this paper, we have presented a method for defect detection in texture images. The novel contribution of our method is the use of a texture feature to construct a prior map, in the low-rank representation framework. Specifically, the proposed method is divided into two steps: calculating the texture prior of an input image; and detecting defects in the low-rank representation with the texture prior map, in which a weighted low-rank model is adopted. The proposed method can handle defective images with simple or complicated texture background and various defects. Experiments on synthetic and real images show that the proposed method is superior to the state-of-the-art defect detection methods in terms of detection accuracy, and that it is competitive in terms of computational time.

However, the limitations of the proposed method should not be ignored. One limitation of the proposed method is that the performance of the method partly depends on the quality of the prior map. When the prior map is not ideal, the detection results might be not acceptable. Another limitation is that the proposed method assumes the defects as foreground. As a result, when the defect is bigger than the background, the method might fail to detect. Our ongoing work also includes improvement of the computational efficiency and application of the proposed method to real-world problems such as the inspection of mobile phone screens and quality control of metallic surface polishing.

REFERENCES

[1] Q. P. Huang, T. Liu, Q. Sun, and W. Huang, "Reliability estimation for aluminum alloy welded joint with automatic image measurement of surface crack growth," *Eng. Comput.*, vol. 33, no. 4, pp. 1205–1223, 2016.
[2] J. Cao, N. Wang, J. Zhang, Z. Wen, B. Li, and X. Liu, "Detection of varied defects in diverse fabric images via modified RPCA with noise term and defect prior," *Int. J. Clothing Sci. Technol.*, vol. 28, no. 4, pp. 516–529, 2016.
[3] A. Kumar, "Computer-vision-based fabric defect detection: A survey," *IEEE Trans. Ind. Electron.*, vol. 55, no. 1, pp. 348–363, Jan. 2008.
[4] V. Asha, N. U. Bhajantri, and P. Nagabhushan, "Similarity measures for automatic defect detection on patterned textures," *Int. J. Inf. Commun. Technol.*, vol. 4, pp. 118–131, Jan. 2012.
[5] T. Qu, L. Zou, Q. Zhang, X. Chen, and C. Fan, "Defect detection on the fabric with complex texture via dual-scale over-complete dictionary," *J. Textile Inst. Proc. Abstr.*, vol. 107, no. 6, pp. 743–756, 2016.
[6] M. Behravan, F. Tajeripour, Z. Azimifar, and R. Boostani, "Texton-based fabric defect detection and recognition," *Iranian J. Elect. Comput. Eng.*, vol. 10, no. 2, pp. 57–69, Jun. 2011.
[7] Y. Park and I. S. Kweon, "Ambiguous surface defect image classification of AMOLED displays in smartphones," *IEEE Trans. Ind. Informat.*, vol. 12, no. 2, pp. 597–607, Apr. 2016.
[8] Y. X. Zhi, G. K. H. Pang, and N. H. C. Yung, "Fabric defect detection using adaptive wavelet," in *Proc. IEEE Int. Conf. Acoust., Speech, Signal Process.*, Salt Lake City, UT, USA, May 2001, doi: 10.1109/ICASSP.2001.940645.
[9] C. Li, G. Gao, Z. Liu, D. Huang, S. Liu, and M. Yu. (2017). "Defect detection for patterned fabric images based on GHOG and low-rank decomposition." [Online]. Available: https://arxiv.org/abs/1702.05555
[10] D. Zhang, G. Gao, and C. Li, "Fabric defect detection algorithm based on Gabor filter and low-rank decomposition," in *Proc. 8th Int. Conf. Digit. Image Process. (ICDIP)*, vol. 10033, Aug. 2016, p. 100330L, doi: 10.1117/12.2244861.
[11] J. Zhou, J. Wang, and H. Bu, "Fabric defect detection using a hybrid and complementary fractal feature vector and FCM-based novelty detector," *Fibres Textiles Eastern Eur.*, vol. 25, no. 6, pp. 46–52, 2017.
[12] D. Zhu and A. A. L. Beex, "Robust spatial autoregressive modeling for hardwood log inspection," *J. Vis. Commun. Image Represent.*, vol. 5, no. 1, pp. 41–51, 1994.
[13] Y. Li, W. Zhao, and J. Pan, "Deformable patterned fabric defect detection with Fisher criterion-based deep learning," *IEEE Trans. Autom. Sci. Eng.* vol. 14, no. 2, pp. 1256–1264, Apr. 2017.
[14] R. Ren, T. Hung, and K. C. Tan, "A generic deep-learning-based approach for automated surface inspection," *IEEE Trans. Cybern.*, vol. 48, no. 3, pp. 929–940, Mar. 2018.
[15] L. Zhang, F. Yang, Y. D. Zhang, and Y. J. Zhu, "Road crack detection using deep convolutional neural network," in *Proc. IEEE Int. Conf. Image Process.*, Sep. 2016, pp. 3708–3712.
[16] Y.-G. Cen, R.-Z. Zhao, L.-H. Cen, L.-H. Cui, Z.-J. Miao, and Z. Wei, "Defect inspection for TFT-LCD images based on the low-rank matrix reconstruction," *Neurocomputing*, vol. 149, pp. 1206–1215, Feb. 2015.
[17] J. Cao, J. Zhang, Z. Wen, N. Wang, and X. Liu, "Fabric defect inspection using prior knowledge guided least squares regression," *Multimedia Tools Appl.*, vol. 76, no. 3, pp. 4141–4157, 2017, doi: 10.1007/s11042-015-3041-3.
[18] X. Zhou, C. Yang, and W. Yu, "Moving object detection by detecting contiguous outliers in the low-rank representation," *IEEE Trans. Pattern Anal. Mach. Intell.*, vol. 35, no. 3, pp. 597–610, Mar. 2013.
[19] S. Z. Li, *Markov Random Field Modeling in Image Analysis*. London, U.K.: Springer-Verlag, 2009.
[20] R. Mazumder, T. Hastie, and R. Tibshirani, "Spectral regularization algorithms for learning large incomplete matrices," *J. Mach. Learn. Res.*, vol. 11, pp. 2287–2322, Mar. 2010.
[21] V. Kolmogorov and R. Zabin, "What energy functions can be minimized via graph cuts?" *IEEE Trans. Pattern Anal. Mach. Intell.*, vol. 26, no. 2, pp. 147–159, Feb. 2004.
[22] X. Ma, X. Xie, K.-M. Lam, J. Hu, and Y. Zhong, "Saliency detection based on singular value decomposition," *J. Vis. Commun. Image Represent.*, vol. 32, pp. 95–106, Oct. 2015, doi: 10.1016/j.jvcir.2015.08.003.
[23] D. Yapi, M. S. Allili, and N. Baaziz, "Automatic fabric defect detection using learning-based local textural distributions in the contourlet domain," *IEEE Trans. Autom. Sci. Eng.*, vol. 15, no. 3, pp. 1014–1026, Jul. 2018.
[24] B. Julesz, "Textons, the elements of texture perception, and their interactions," *Nature*, vol. 290, no. 5802, pp. 91–97, 1981.

QIZI HUANGPENG received the B.S. and M.S. degrees in management science and engineering from the National University of Defense Technology, Changsha, Hunan, China, in 2013 and 2015, respectively, where she is currently pursuing the Ph.D. degree with the Department of System Engineering. Her research interests include image processing, pattern recognition, and visual defect detection.

HONG ZHANG received the B.Sc. degree in electrical and computer engineering from Northeastern University, Boston, MA, USA, and the Ph.D. degree in electrical and computer engineering from Purdue University, West Lafayette, IN, USA. He is currently a Professor with the Department of Computing Science, University of Alberta, and the Director of the Centre for Intelligent Mining Systems. His current research interests include robotics, computer vision, image processing, and intelligent systems. He is a fellow of the Canadian Academy of Engineering.

XIANGRONG ZENG received the B.S. degree in management engineering and the M.S. degree in system engineering from the National University of Defense Technology, Changsha, Hunan, China, in 2008 and 2010, respectively, and the Ph.D. degree in electrical and computer engineering from the Instituto Superior Tecnico, Universidade de Lisboa, Portugal, in 2015. He is currently an Assistant Professor with the Department of System Engineering, College of Information System and Management, National University of Defense Technology. His current research interests include compressed sensing, computational photography, and convex optimization methods in signal and image processing.

WENWEI HUANG received the B.S. degree from the Military Engineering College of Changsha in 1983 and the M.S. degree from Hunan Normal University in 1990. He is currently a Professor with the National University of Defense Technology. His research interests include image processing and data mining.